Active mechanics of sea star oocytes

Peter J. Foster[1,†,*], Sebastian Fürthauer[2,3,*], Nikta Fakhri[1,*]

[1] Physics of Living Systems, Department of Physics, Massachusetts Institute of Technology, Cambridge, MA, 02139, USA
[2] Institute for Applied Physics, TU Wien, A-1040 Wien, Austria
[3] Center for Computational Biology, Flatiron Institute, New York, NY, 10010, USA
† Present address: Department of Physics, Brandeis University, Waltham, MA, 02454, USA
* For correspondence; foster@brandeis.edu (PJF); fuerthauer@iap.tuwien.ac.at (SF); fakhri@mit.edu (NF)

Abstract

Actomyosin is a canonical example of an active material, driven out of equilibrium in part through the injection of energy by myosin motors. This influx of energy allows actomyosin networks to generate cellular-scale contractility, which underlies cellular processes ranging from division to migration. While the molecular players underlying actomyosin contractility have been well characterized, how cellular-scale deformation in disordered actomyosin networks emerges from filament-scale interactions is not well understood. Here, we address this question *in vivo* using the meiotic surface contraction wave of *Patiria miniata* oocytes. Using pharmacological treatments targeting actin polymerization, we find that the cellular deformation rate is a nonmonotonic function of cortical actin density peaked near the wild type density. To understand this, we develop an active fluid model coarse-grained from filament-scale interactions and find quantitative agreement with the measured data. This model further predicts the dependence of the deformation rate on the concentration of passive actin crosslinkers and motor proteins, including the surprising prediction that deformation rate decreases with increasing motor concentration. We test these predictions through protein overexpression and find quantitative agreement. Taken together, this work is an important step for bridging the molecular and cellular length scales for cytoskeletal networks *in vivo*.

Introduction

Actomyosin networks are canonical examples of living active materials, which generate nonequilibrium active stresses enabled by the energy injected by the system's constituent components [1–5]. While the mechanisms underling contractility in structurally ordered actomyosin networks, such as in muscle sarcomeres, is well understood, the mechanisms underlying the contractility of disordered actin networks such as the cortex remains poorly understood [6–8]. Contractility in disordered actomyosin networks has been shown to depend not solely on myosin activity, but on the the architecture [8, 9] and density [10] of the actin network. Additionally, a substantial body of work in *in vitro* systems has demonstrated that in many cases F-actin and myosin alone are insufficient for network contractility and that additional actin crosslinking proteins are required [11–15], though an exception has been found at low pH where myosin itself can function as an effective crosslinker [16].

Understanding how the cellular-scale properties of actomyosin networks emerge from the filament-scale interactions of the network's constituents is an open challenge. To generate contractile stresses, the filament-scale symmetry between contraction and expansion must be broken [17]. A number of microscopic models have been proposed for how this symmetry can be broken [8, 18]. One class of models relies on polarity sorting - myosin accumulates at actin barbed ends, clustering barbed ends together which in turn leads to isotropic contraction [19]. Myosin-2 end accumulation has been demonstrated in a purified system [7], and this mechanism has been argued to give rise to contraction in microtubule networks [20–22]. Alternatively, contractility has been proposed to arise from the nonlinear mechanical properties of F-actin, which can buckle under compression. In purified systems, F-actin buckling has been seen to coincide with network contraction, [15, 23]. Finally, contractility independent of myosin motor activity has been proposed for some structures, such as the contractile F-actin shell that captures chromosomes during sea star oocyte meiosis [24–28]. However, directly assessing the degree of myosin end accumulation or filament buckling *in vivo* presents an experimental challenge due to the high density and small size of myosin and actin filaments, which limits the ability to resolve individual motors and filaments using light microscopy.

Here, we consider the actomyosin-driven surface contraction wave of meiotic *Patiria miniata* oocytes as a model for cellular contractility. Using pharmacological inhibitions targeting actin polymerization dynamics, we find that cellular deformation during the contraction wave is not a monotonic function of cortical actin density, but is instead peaked near the wild type density. To understand this phenomenon, we utilize a recently developed theoretical framework for dense cytoskeletal networks [29] that generalizes a model developed for microtubule networks [30] to allow for more elaborate motor and crosslinker properties. Based on this, we develop an active fluid model coarse grained from a microscopic description of actin, crosslinkers, and motors. This model makes quantitative predictions for how the rate of oocyte deformation varies with the concentrations of passive active crosslinkers and active motor proteins, namely that the radial deformation rate slightly increases before decreasing as passive crosslinker concentration increases, and surprisingly, decrease with increasing active motor concentration. We compare these predictions with experimental measurements from oocytes overexpressing α-actinin or myosin regulatory light chain and find quantitative agreement. Taken together, these results provide a step towards quantitatively bridging length scales, from filament-level interactions to the emergent mechanics of actomyosin structures *in vivo*.

Results

Surface contraction wave dynamics

As a model process for actomyosin-driven contraction *in vivo*, we here consider the surface contraction wave preceding the first meiotic division in oocytes of the bat star *Patiria miniata* [31–33]. First discovered in developing axolotl [34], surface contraction waves are found in a variety of large eggs

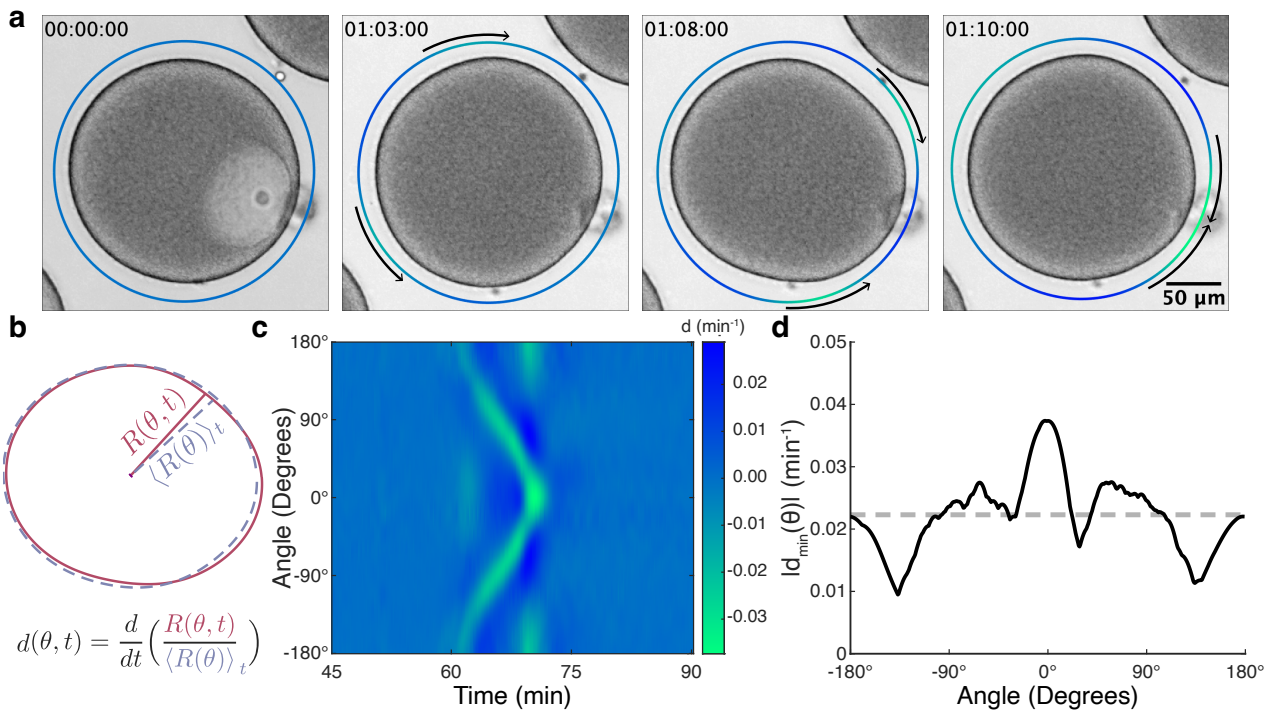

Figure 1: Surface contraction wave dynamics. (a) Timelapse of oocyte surface contraction wave. The outer circle color denotes $d(\theta, t)$, the radial deformation rate for each angle, colored as in c. Negative (green) values indicate contraction while positive (dark blue) values indicate expansion. Arrows indicate the direction of wave propagation. (b) Deformation rate calculation. For each angle at each time, the radial distance between the oocyte's centroid and outer contour was normalized by the time averaged radial distance before a time derivative was taken. (c) Kymograph of $d(\theta, t)$. The surface contraction wave is readily visualized as the converging lines of negative (green) values indicating contraction. (d) Solid line: Magnitude of the minimum deformation rate for each angle, $d_{min}(\theta)$. Dashed line: d_c, the average value of $|d_{min}(\theta)|$.

including those of the frog *Xenopus laevis* [35], barnacles [36], and ascidians [37]. In sea star oocytes, these waves are driven by a band of activated Rho that travels across the oocyte from the vegetal to animal pole, guided by a spatial gradient of cdk1-cyclinB [31, 33]. This traveling band of active Rho locally activates several downstream factors, including myosin via the ROCK pathway and the actin nucleator formin mDia1 [38]. These in turn lead to local contraction, resulting in a traveling surface contraction wave (SCW), whose arrival at the animal pole coincides with polar body extrusion [31, 32](Fig. 1a, Supplementary Video 1). Due to the ease of meiotic induction, the large, spherical shape of sea star oocytes, and the highly conserved nature of the actomyosin components [17], sea star oocytes are a powerful model system for the study of actomyosin contractility *in vivo*. While a surface contraction wave coincides with each meiotic division, we here consider the first surface contraction wave which takes place during meiosis i.

We first quantified a characteristic radial deformation rate and the wave propagation speed during the SCW. To quantify the deformation rate, the distance between the oocyte's center and outer contour at each angle and time point, $R(\theta, t)$ was first normalized by the time averaged radial distance for that angle, $\langle R(\theta)\rangle_t$ and a time derivative was taken to compute the local deformation rate, $d(\theta, t)$ (Fig. 1b, see *Materials and Methods*). From kymographs of $d(\theta, t)$, the SCW can be readily visualized as a traveling line of negative values (Fig. 1c), and the propagation speed of the

wave can be measured from the slope of this line (see *Materials and Methods*). A characteristic deformation rate was calculated by first taking the magnitude of the minimum deformation rate for each angle, $|d_{min}(\theta)|$ (Fig. 1d, solid line) which was then averaged across angles to determine the characteristic deformation rate, $d_c = \langle |d_{min}(\theta)| \rangle_\theta$ (Fig. 1d, dashed line, see *Materials and Methods*). Control oocytes were found to have a mean wave propagation speed of $v = 47 \pm 4\ \mu m/min$ (mean ± s.e.m., n=25 oocytes), consistent with previous measurements [31], and a characteristic deformation rate of $d_c = 0.017 \pm 0.002$ min $^{-1}$ (mean ± s.e.m., n=25 oocytes).

Characteristic deformation rate is maximum at intermediate cortical actin density

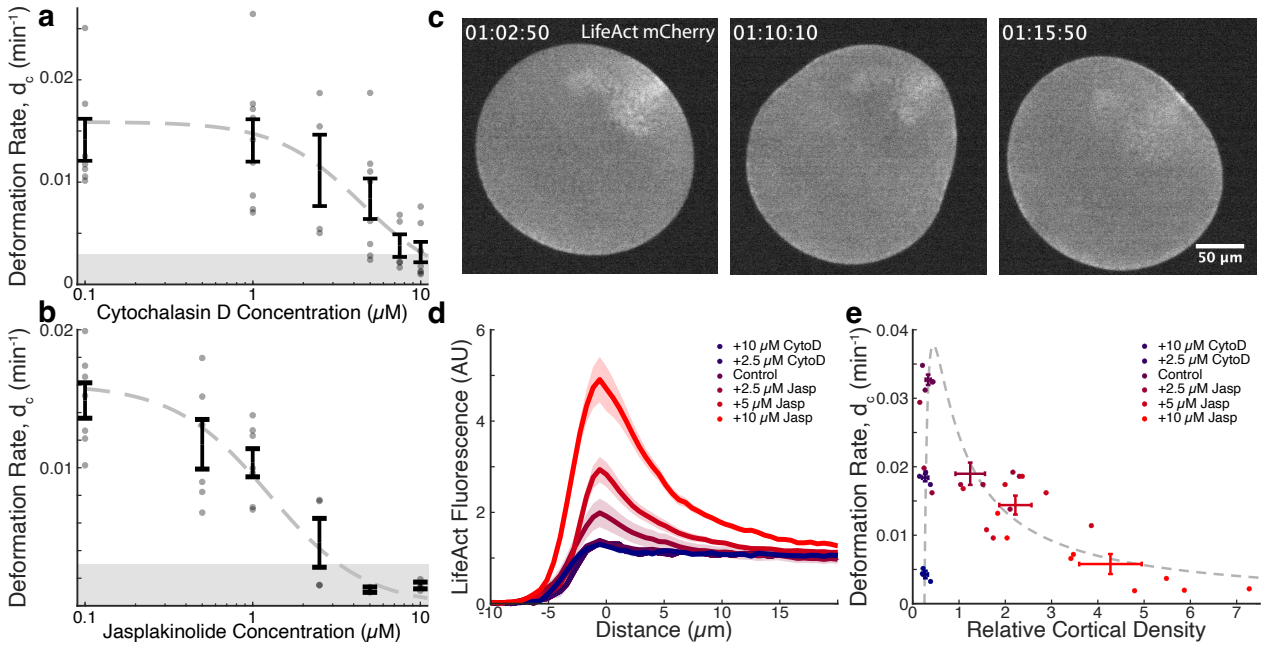

Figure 2: Characteristic deformation rate is maximized at intermediate actin density (a,b) Average characteristic deformation rate, d_c, as a function of cytochalasin D and jasplakinolide. Gray dots: measurements from individual oocytes. Black lines: average deformation rate ± s.e.m. Gray regions: noise floor. Dashed line: IC50 fits. Cytochalasin D experiments: n=4 to n=9 oocytes per treatment condition. Jasplakinolide experiments: n=2 to n=7 oocytes per treatment condition (c) LifeAct-mCherry imaging of F-actin localization during maturation (d) Average normalized radial line profiles of LifeAct-mCherry fluorescence for varying cytochalasin D and jasplakinolide concentrations (mean ± s.e.m.). (e) Characteristic deformation rate, d_c, as a function of relative cortical density. Errorbars: mean ± s.e.m. for each treatment condition. Grey dashed line: model fit

We next investigated how modulating actin density through perturbing actin turnover influences deformation dynamics during the SCW. We first considered the actin polymerization inhibitor cytochalasin D, which at high concentrations has been shown to inhibit deformation during the SCW [31]. Measurements of the characteristic deformation rate, d_c, and the wave speed, v, were repeated for oocytes treated with varying concentrations of cytochalasin D. As expected for an actomyosin-driven process, the characteristic deformation rate was found to monotonically decrease with increasing cytochalasin D concentration (Fig. 2a). Fitting a dose response curve yielded an IC_{50} of $4.4 \pm 2.0\ \mu$M (fit value ± 95% confidence interval, see *Materials and Methods*). For concentrations of cytochalasin D $\leq 5\ \mu$M, where deformation during the SCW was large enough for the wave speed to be measured, no significant differences in wave speed were found between treatment conditions (Extended Data Figure 1), consistent with previous results arguing that the speed of the SCW is

set by the spatiotemporal dynamics of cdk1-cyclinB [31, 33].

We next considered the effects of jasplakinolide, which induces actin polymerization and stabilization [39]. Surprisingly, we found a dose-dependent decrease in the characteristic deformation rate (Fig. 2b). Fitting a dose response curve yielded an IC_{50} of $1.3 \pm 0.8\mu$M (fit value $\pm$ 95% confidence interval, see *Materials and Methods*). Thus, treatment with drugs which either suppress or promote actin polymerization reduce the characteristic deformation rate during the SCW.

To quantitatively assess how these perturbations modulate actin density, we next overexpressed and imaged LifeAct-mCherry and used its fluorescence intensity as a proxy for F-actin density (see *Materials and Methods*). As expected, LifeAct-mCherry localized to the oocyte's periphery and to the nuclear region shortly after the onset of nuclear envelope breakdown, (Fig. 2c), consistent with F-actin's role in nuclear envelope breakdown in sea star oocytes [40, 41]. As time progresses, the cortical LifeAct-mCherry signal globally decreases before locally increasing slightly during the surface contraction wave (Fig. 2c, Supplementary Video 2).

To characterize the cortical actin density, line scans of LifeAct fluorescence were measured midway between the animal and vegetal poles when the SCW passed through this region, and the intensity profiles interior to the cell were fit to a decaying exponential function $I(r) = I_0 e^{-r/\lambda} + I_C$. The relative cortical density (RCD) was then calculated from these fitting parameters as $RCD = I_0/(I_C - I_{BG})$, where I_{BG} is the average fluorescence signal exterior to the cell (see *Materials and Methods*). Measurements of the relative cortical density and characteristic radial deformation rate were performed for individual oocytes treated with varying concentrations of cytochalasin D or jasplakinolide, allowing a direct comparison between the effects of these two treatments (Fig. 2d). As anticipated from the measured dose response curves (Fig. 2a,b), we find that the characteristic deformation rate is not a monotonic function of cortical actin density, but instead sharply increases before slowly decreasing with increasing cortical actin density, with a peak near the wild-type density (Fig. 2e).

An active fluid model coarse-grained from microscopic interactions

To understand the origin of the observed dependence of the radial deformation rate on actin density, it is useful to first consider the force balance of the material on long timescales, which follows,

$$\nabla_j \left(\eta_{ijkl} \nabla_k \mathbf{v}_l + \Sigma^A \delta_{ij} + \mathcal{T}_{ij} \right) = 0 \tag{1}$$

where η_{ijkl} is the viscosity tensor where the nonzero elements take the form $\eta_{ijkl} = \eta \xi_{ijkl}$, where η is the magnitude of the dominant component of the viscosity and ξ_{ijkl} encodes geometric information and scalings, Σ_A is the active stress generated by interactions between actin filaments, molecular motors, and passive crosslinkers, and $\mathcal{T}$ is a passive stress arising from surface tension. Einstein's convention of summation over repeated indices is implied. Eqn. 1 can be mapped to a thin spherical shell of material (see Supplementary Information), yielding that the rate of deformation in the radial direction scales with the active stress, Σ_A, and the inverse of the viscosity, η, and thus $d \simeq ||\Sigma_A/\eta||$. To obtain predictions for the dependence of η and Σ_A on the actin density, we adapted a recently developed theoretical framework which allows a microscopic description of the system to be coarse-grained into an emergent mechanical model [29]. An application of this general framework to the actomyosin system considered here begins with a simplified microscopic description of the system and considers three elements: actin filaments, passive crosslinkers, and molecular motors.

Molecular motors and passive crosslinkers exert forces between the filaments which they connect. For passive crosslinkers, these forces are taken to be proportional to the velocity difference between the points on the actin filament connected by the crosslinker. Thus, for a single crosslinker bound

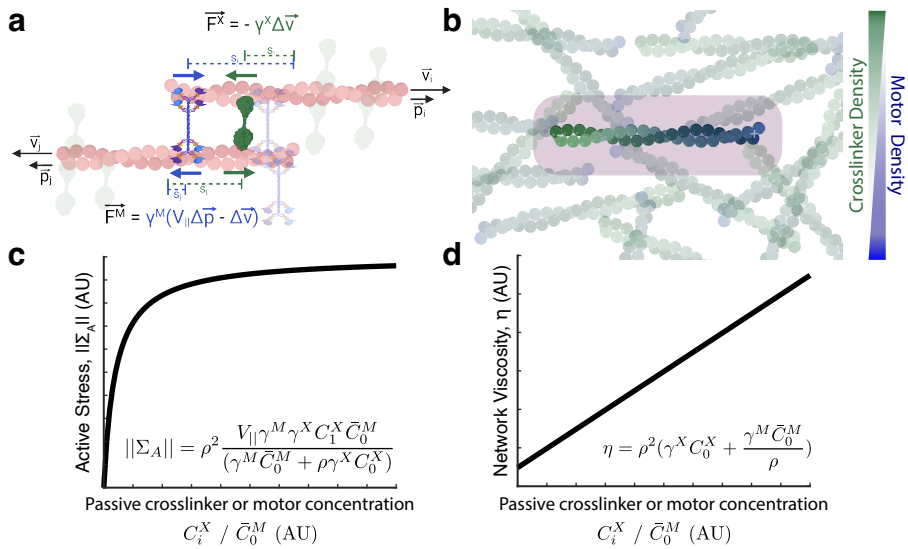

Figure 3: Active fluid model (a) Schematic of filament-scale forces between antiparallel actin filaments from individual motors (blue) and passive crosslinkers (green). (b) In the model considered in the main text, motors (blue) are uniformly distributed on actin filaments, while passive crosslinkers (green) accumulate near the filament end they motor walks away from. (c,d) Functional forms of the scalings of the active stress magnitude, $||\Sigma_A||$, (c) and the viscosity, η, (d) with the concentrations of either passive crosslinkers (C_i^X) or motors ($\bar{C}_0^M$).

between position s_i on the i-th actin filament and s_j on the j-th filament, the force exerted between filaments is given by

$$\mathbf{F}_{ij}^X = -\gamma^X(\mathbf{v}_i + s_i\dot{\mathbf{p}}_i - \mathbf{v}_j - s_j\dot{\mathbf{p}}_j), \tag{2}$$

where $\mathbf{v}_i$ and $\mathbf{p}_i$ are the velocity and direction of filament i, and γ^X describes the coupling strength (see Fig. 3a). When multiple passive crosslinkers are bound between filament pairs, the net force exerted between filaments becomes,

$$\mathbf{f}_{ij}^X = -\gamma^X c^X(s_i, s_j)(\mathbf{v}_i + s_i\dot{\mathbf{p}}_i - \mathbf{v}_j - s_j\dot{\mathbf{p}}_j), \tag{3}$$

where $c^X(s_i, s_j)$ is the number of passive crosslinkers that are bound between positions s_i and s_j, which can spatially vary along filaments. Motor molecules likewise contribute to the frictional coupling between filaments, but due to their stepping motion along filaments, exert additional active forces. The net force exerted by motors between filaments, $\mathbf{f}_{ij}^M$ can be written as,

$$\mathbf{f}_{ij}^M = -\gamma^M c^M(s_i, s_j)\Big(\mathbf{v}_i + s_i\dot{\mathbf{p}}_i - \mathbf{v}_j - s_j\dot{\mathbf{p}}_j + V_{||}(\mathbf{p}_i - \mathbf{p}_j)\Big). \tag{4}$$

where the coefficient $V_{||}$ is the unloaded speed of the motor, γ^M is the motor friction, and $c^M(s_i, s_j)$ is the density of motor molecules connecting two specific filament positions. We further postulate functional forms for the motor and crosslinker densities,

$$c^M(s_i, s_j) = C_0^M + (s_i + s_j)C_1^M \tag{5}$$

$$c^X(s_i, s_j) = C_0^X + (s_i + s_j)C_1^X$$

where C_0^M, C_0^X represent the number of uniformly bound motors and crosslinkers, and C_1^M and C_1^M capture nonuniformity of binding along filaments. Given Eqns. 3, 4, and 5, predictions for η and

Σ_A, can be derived by integrating over all possible configurations of motors and crosslinkers [29] (Fig. 3b, see Supplementary Information). The viscosity of the system is predicted to be

$$\eta \propto \rho^2(\gamma^X C_0^X + \gamma^M C_0^M) \tag{6}$$

Furthermore, the active stress is predicted to be,

$$\Sigma_A \propto \rho^2 \gamma^M V_{||} \left(C_1^M - C_0^M \frac{\gamma^M C_1^M + \gamma^X C_1^X}{\gamma^M C_0^M + \gamma^X C_0^X} \right), ; \tag{7}$$

With this, the contraction rate is expected to be,

$$d = \frac{\Sigma_A}{\eta} = \gamma^M V_{||} \frac{C_1^M - C_0^M \frac{\gamma^M C_1^M + \gamma^X C_1^X}{\gamma^M C_0^M + \gamma^X C_0^X}}{\gamma^M C_0^M + \gamma^X C_0^X}. \tag{8}$$

To relate these results to our experimental findings we next need to specify how C^M and C^X change as a function of actin density, ρ. A number of simple microscopic models are possible, and we here consider a model where passive crosslinkers accumulate near the filament ends motors walk away from, while motors are uniformly distributed along filaments, i.e. $C_1^M = 0$ (see Supplemental Information for a discussion of other microscopic models). Such a configuration of passive crosslinkers is consistent with filament crosslinking by the Arp2/3 complex, which localizes to the pointed end of daughter filaments while nonmuscle myosin II walks towards the barbed end. We assume that the total number of bound passive crosslinkers is limited by the number of available binding sites, and thus the per filament amounts of passive crosslinkers C_0^X and C_1^X are independent of ρ. We further propose that binding of motors is limited by the available concentration of active motors in the system. Thus, as the system becomes denser and ρ increases, the amount C_0^M of motors per filament decreases, i.e. $C_0^M = \bar{C}_0^M/\rho$, where $\bar{C}_0^M$ is a constant total amount of available motor. This finally leads to

$$||d|| = \frac{\alpha\rho}{(1+\beta\rho)^2} \tag{9}$$

where $\alpha = V_{||}\frac{\gamma^X C_1^X}{\gamma^M \bar{C}_0^M}$, $\beta = \frac{\gamma^X C_0^X}{\gamma^M \bar{C}_0^M}$, and ρ is the actin density. We note that this mechanical model arises for a particular choice of microscopic model, and other choices of microscopic models that are consistent with the experimental measurements presented here lead to differing functional forms for the dependence of α and β on model parameters (see Discussion, Supplementary Information).

We first asked whether the active fluid model reproduces the observed changes in the characteristic radial deformation rate as the cortical actin density is varied (Fig. 2e). To compare with experimental data, we correct for a constant offset in the measured cortical densities, ρ_0, and fit

$$d_c = \frac{\alpha(\rho - \rho_0)}{\left(1 + \beta(\rho - \rho_0)\right)^2} \tag{10}$$

Such an offset could potentially arise from a loss of global network contractility at finite density, perhaps due to a loss in network connectivity [14]. Fitting Eqn. 10. to the average characteristic radial deformation rate and relative cortical actin density for each treatment condition provides excellent quantitative agreement with the measured data (Fig. 2e) and provides measurements of the underlying model parameters, $\alpha = 0.8 \pm 1.0\ min^{-1}$, $\beta = 5.2 \pm 5.7$, and $\rho_0 = 0.25 \pm 0.04$ (fit values $\pm$ 95% confidence intervals).

Testing the active fluid model through protein inhibition and overexpression

The active fluid model is based on a microscopic model where forces are generated by the activity of molecular motors. We first sought to test this assumption and confirm that myosin activity underlies deformation during the SCW by treatment with the myosin inhibitor blebbistatin, which has

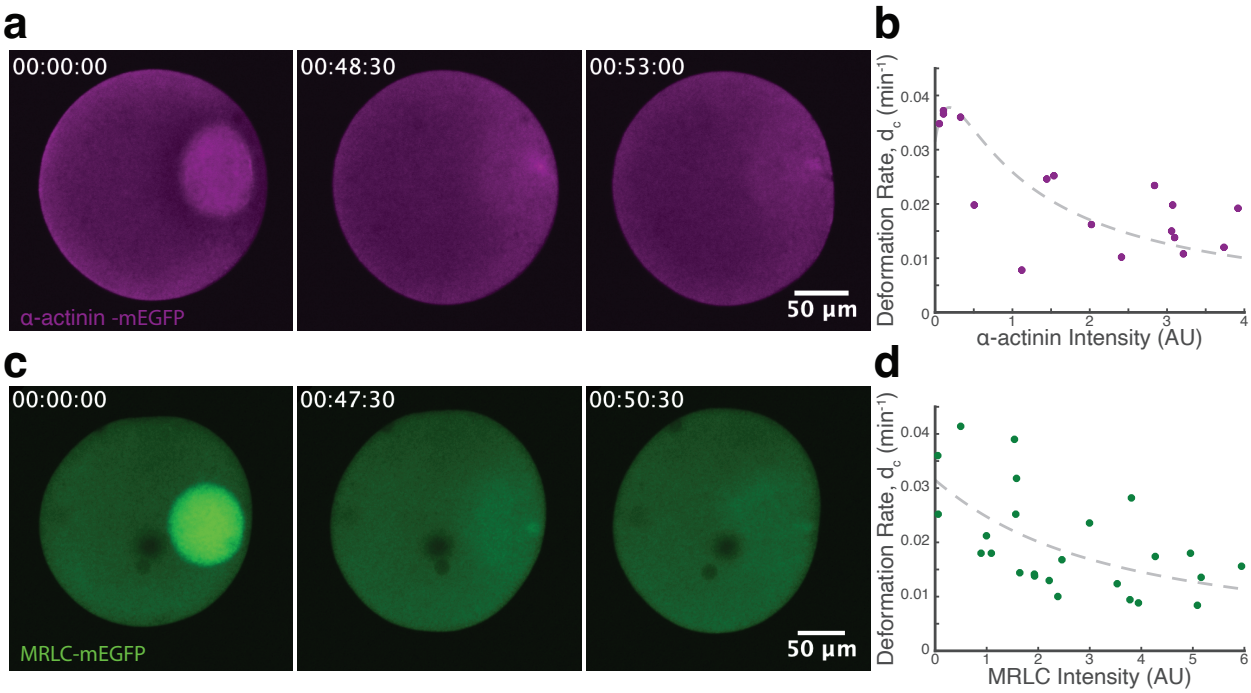

Figure 4: Crosslinker and motor overexpression to test active fluid model predictions. (a) Timecourse of SCW for an oocyte overexpressing α-actinin-mEGFP. (b) Characteristic deformation rate as a function of α-actinin-mEGFP intensity (n=17 oocytes). (c) Timecourse of SCW for an oocyte overexpressing MRLC-mEGFP. (d) Characteristic deformation rate as a function of MRLC-mEGFP intensity (n=25 oocytes). Grey dashed line: model fit

previously been shown to almost completely suppress contraction during the SCW [31]. We find that treatment with 200 μM blebbistatin substantially decreases the characteristic deformation rate, consistent with myosin's role in driving contraction (Extended Data Figure 2).

To further test the active fluid model, we next performed experiments increasing the concentration of either a passive actin crosslinking protein or an active motor. In the active fluid model, the viscosity, η, and the active stress magnitude, $||\Sigma_A||$ are predicted to scale differently when the concentrations of either passive crosslinker or active motors are varied (Fig. 3c,d, Eqns. 6, 7). The concentrations of passive crosslinkers and motor proteins enter the characteristic deformation rate through the coefficients α and β, which are both proportional to $\frac{C_i^X}{\overline{C}_0^M}$. Thus, for a fractional change in the total passive crosslinker concentration, f, α and β are predicted to change as,

$$\begin{aligned} \tilde{\alpha} =& \alpha(1+f) \\ \tilde{\beta} =& \beta(1+f) \end{aligned} \tag{11}$$

To test this prediction, we overexpressed an actin crosslinking protein in untreated oocytes. While a variety of passive actin crosslinkers localize to the cortex [42], we here use α-actinin. Fluorescent mEGFP-labeled *Patiria miniata* α-actinin [40] was overexpressed by injecting oocytes with the corresponding mRNA (see *Materials and Methods*), and we make use of the natural variability in protein expression level to assess changes in the characteristic radial deformation rate over a range of α-actinin concentrations.

Characteristic deformation rates and the fluorescence signals of α-actinin-mEGFP, which we use as a proxy for α-actinin concentration, were measured for individual oocytes (Fig. 4a, Supplementary

Video 3). Overall, we find a general trend of decreasing deformation rate with increasing levels of α-actinin overexpression, qualitatively consistent with the prediction of the active fluid model. To quantitatively test the model, we take the actin density to be the previously measured wild-type value, $\rho = \rho_{WT}$ and relate the measured α-actinin-mEGFP fluorescence signal to the fractional change in passive crosslinker concentration as,

$$f = \chi_{actinin} I_{actinin} \tag{12}$$

Using values for α, β, and ρ_0 taken from the fit of characteristic deformation rate vs. relative cortical density (Fig. 2e), Eqns. 10, 11, 12 were combined and fit to the experimental data, and found to be in quantitative agreement, providing a measure of the sole fit parameter, $\chi_{actinin} = 7.5 \pm 2.8$ (fit value $\pm$ 95% confidence interval).

The active fluid model further predicts how the characteristic deformation rate should change with the concentration of active motors. In this model, motors contribute both active forces and an effective friction between sliding filaments. As such, changes in the concentration of motor proteins are predicted to change both the emergent active stress and network viscosity. While for low motor concentrations the model predicts that the deformation rate will increase with increasing motor concentration, at sufficiently high motor concentrations this model predicts that network viscosity will grow faster than active stress, and hence the deformation rate will instead decrease with increasing motor concentration (Fig. 4c,d).

To experimentally test this prediction, mEGFP-labeled *Patiria miniata* myosin regulatory light chain (MRLC) was overexpressed in oocytes (Fig. 5c, Supplementary Video 4). MRLC overexpression in *Patiria miniata* oocytes has previously been shown to increase the strength of the SCW [27, 31] and to increase nonequilibrium activity in the cortex [43]. Following the same logic as for α-actinin overexpression, we note that both α and β scale inversely with the per filament motor concentration, and the measured MRLC-mEGFP fluorescence signal can be related to the fractional change in motor concentration,

$$\begin{aligned} \bar{\alpha} &= \frac{\alpha}{(1 + \chi_{MRLC} I_{MRLC})} \\ \bar{\beta} &= \frac{\beta}{(1 + \chi_{MRLC} I_{MRLC})} \end{aligned} \tag{13}$$

The characteristic deformation rate and MRLC-mEGFP fluorescence were measured for individual oocytes (see *Materials and Methods*) and the resulting data was fit to Eqns. 10, 13. Once again, using only a single free fitting parameter, χ_{MRLC}, we find quantitative agreement between the measured data and the prediction of the active fluid model (Fig. 4d), providing a measure of $\chi_{MRLC} = 0.6 \pm 0.3$ (fit value $\pm$ 95% confidence interval).

In the context of the active fluid model considered here, one key control parameter, $\zeta = \frac{\gamma^X C_0^X (\rho - \rho_0)}{\gamma^M \bar{C}_0^M}$, determines the sample composition that maximizes the deformation rate. By using the fit parameters α, β, $\chi_{actinin}$, and χ_{MRLC}, data for the actin density, α-actinin overexpression, and MRLC overexpression experiments (Figs. 2e, 4b, and 4d) can be reparameterized and plotted as a function of ζ. When plotted in this way, the data are found to collapse to the curve predicted by the active fluid model (Fig. 5).

Discussion

Here, we used surface contraction waves in maturing sea star oocytes as a model to study actomyosin contractility *in vivo*. By controlling cortical actin density, we find that the deformation rate is max-

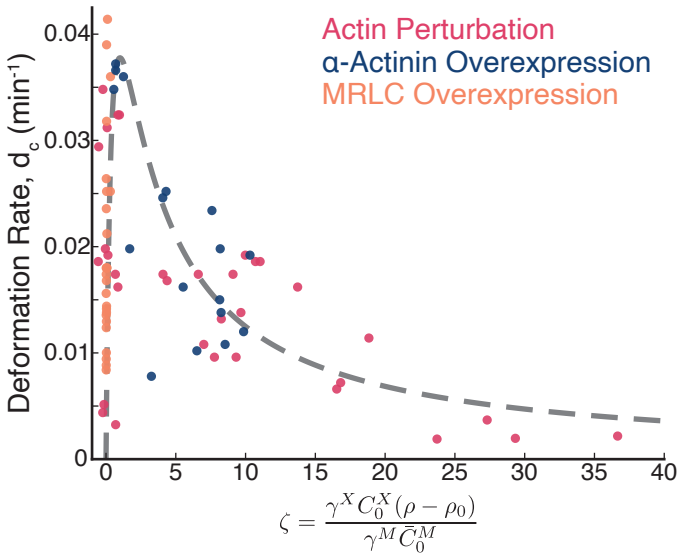

Figure 5: Using the fit parameters α, β, ρ_0, $\chi_{actinin}$, and χ_{MRLC}, data from experiments with varying Relative Cortical Density (Fig. 2e), α-actinin-mEGFP concentration (Fig. 4b), and MRLC-mEGFP concentration (Fig. 4d) can be reparameterized and plotted as a function of the model parameter $\zeta = \frac{\gamma^X C_0^X (\rho - \rho_0)}{\gamma^M \bar{C}_0^M}$. Upon replotting, the data collapse to a curve predicted by the active fluid model.

imum near the wild-type density and decreases when the cortical actin density is either increased or decreased. To understand this phenomenon, we developed an active fluid model coarse-grained from a microscopic description of the system. The model makes additional predictions for the dependence of the radial deformation rate on passive crosslinker and motor concentrations, which are in quantitative agreement with experimental measurements. Finally, by using model parameters measured from fitting the active fluid model to the actin density, α-actinin overexpression, and MRLC overexpression data, data from all three sets of experiments could be reparameterized and plotted as a function of the same parameter, leading to data collapse to a curve predicted by the active fluid model.

While here we focused on a microscopic model with an Arp2/3-like crosslinker and a uniformly distributed motor whose per-filament concentration scales inversely with actin density, we stress that other models are also consistent with the data presented here. These include models where passive crosslinkers are uniformly distributed on filaments while myosin accumulates towards the end it walks towards, as has been observed *in vitro* [7], and a combination of these models where myosin and passive crosslinkers accumulate at opposite ends. The unifying feature of these models is the broken symmetry between contraction and extension at the filament scale, which requires either an asymmetry in the driving force (due to the spatial localization of motors) or in the frictional coupling (due to the spatial localization of passive crosslinkers). Discriminating between these competing models *in vivo* is a challenge that will require measuring the localization asymmetry of motors and crosslinkers in the cortex.

Similar to previous *in vitro* observations of contractile actomyosin [11, 12, 44], both the *in vivo* measurements and the active fluid model presented here show a decrease in network contractility with increasing crosslinker concentration. In contrast to previous work, the results here show that at high motor concentration, network contractility decreases, a qualitatively different behavior from both previous *in vitro* measurements [11, 45] and theoretical predictions from a filament buckling model [46], where the network contraction rate instead saturates with increasing motor concentration.

Network connectivity has been used to explain previous *in vitro* observations: at low connectivity motor forces cannot propagate to larger scales [14], while at high connectivity network contractility decreases due to either a substantial increase in network rigidity [1, 47] or to a decrease in filament buckling [12, 46]. The active fluid model offers an alternative mechanism that can lead to this phenomenon. At low crosslinker concentrations, active stress falls off faster that viscosity, and thus the network deformation rate decreases. Measuring the network connectivity of *in vivo* actin cortices is a challenge, and in the future electron microscopy could potentially be used to measure whether or not our experimental results at low actin density are above the percolation threshold. At high crosslinker concentration, the model predicts viscosity increases faster than active stress, and hence the deformation rate decreases. This idea shares similarities with models where increased network connectivity leads to high stiffness: both would emerge from a high degree of filament crosslinking. An intriguing possibility is that both classes of models are limiting cases of a universal mechanical framework. Exploring this possibility will be an exciting avenue for future research.

Finally, we note that in the system considered here, the deformation rate is maximal near the wild type composition, and perturbing the system through changing the cortical actin density, α-actinin concentration, or MRLC concentration largely only decreases the deformation rate. For the model considered in the main text, the maximal deformation rate is given by $d_{max} = \frac{V_{||}C_1^X}{4C_0^X}$, implying that increasing the deformation rate further would only be possible through either increasing the relative asymmetry of crosslinker localization or increasing the motor walking speed. Increasing the motor walking speed or changing the system composition would have energetic consequences and energetic considerations can impose additional constraints in living nonequilibrium systems [48]. Understanding the energetic constrains of the emergent dynamics could further constrain possible microscopic models, and would require going beyond network architecture towards a thermodynamic description of such living active systems [5].

Data and Code Availability

All data that support the plots within this paper and other findings of this study are available from the corresponding authors upon reasonable request. Images were analyzed using custom written MATLAB code available at `https://github.com/foster61012/Starfish_SCW`.

Competing Interests

The authors declare no competing interests.

Author Contributions

P.J.F. and N.F. initiated the project and designed the experiments. P.J.F. performed the experiments and analysed the experimental data. S.F. designed the active fluid model. All authors participated in interpreting the experimental and theoretical results and in writing the manuscript.

Acknowledgments

This research was supported by the National Science Foundation CAREER Award to N.F.. P.J.F. acknowledges support from the Gordon and Betty Moore Foundation as a Physics of Living Systems Fellow through grant no. GBMF4513. P.J.F. acknowledges support from the NSF MRSEC DMR-2011846. S.F. acknowledges support from the Vienna Science and Technology Fund (WWTF) and the City of Vienna through project VRG20-002. Fig. 3a,b and Fig. S2 were created with BioRender.com.

References

1. Banerjee, S., Gardel, M. L. & Schwarz, U. S. The Actin Cytoskeleton as an Active Adaptive Material. *Annu Rev Condens Matter Phys* **11,** 421–439 (2020).
2. Foster, P. J., Fürthauer, S., Shelley, M. J. & Needleman, D. J. From cytoskeletal assemblies to living materials. *Curr. Opin. Cell Biol.* **56,** 109–114 (2019).
3. Marchetti, M. C. *et al.* Hydrodynamics of soft active matter. *Reviews Of Modern Physics* **85,** 1143–1189 (2013).
4. Needleman, D. & Dogic, Z. Active matter at the interface between materials science and cell biology. *Nature reviews materials* **2,** 1–14 (2017).
5. Bowick, M. J., Fakhri, N., Marchetti, M. C. & Ramaswamy, S. Symmetry, Thermodynamics, and Topology in Active Matter. *Phys. Rev. X* **12,** 010501 (Feb. 2022).
6. Lenz, M. Reversal of contractility as a signature of self-organization in cytoskeletal bundles. *eLife* **9,** e51751 (2020).
7. Wollrab, V. *et al.* Polarity sorting drives remodeling of actin-myosin networks. *Journal of Cell Science* **132,** jcs219717–14 (2018).
8. Koenderink, G. H. & Paluch, E. K. Architecture shapes contractility in actomyosin networks. *Current Opinion in Cell Biology* **50,** 79–85 (2018).
9. Chugh, P. *et al.* Actin cortex architecture regulates cell surface tension. *Nature Cell Biology* **19,** 689–697 (2017).
10. Feld, L. *et al.* Cellular contractile forces are nonmechanosensitive. *Science Advances* **6,** eaaz6997 (Apr. 2020).

11. Bendix, P. M. *et al.* A Quantitative Analysis of Contractility in Active Cytoskeletal Protein Networks. *Biophysical Journal* **94,** 3126–3136 (2008).

12. Ennomani, H. *et al.* Architecture and Connectivity Govern Actin Network Contractility. *Current Biology* **26,** 616–626 (Mar. 2016).

13. Tan, T. H. *et al.* Self-organized stress patterns drive state transitions in actin cortices. *Science Advances* **4,** eaar2847 (2018).

14. Alvarado, J., Sheinman, M., Sharma, A., MacKintosh, F. C. & Koenderink, G. H. Molecular motors robustly drive active gels to a critically connected state. *Nat. Phys.* **9,** 591–597 (Aug. 2013).

15. Murrell, M. P. & Gardel, M. L. F-actin buckling coordinates contractility and severing in a biomimetic actomyosin cortex. *Proceedings Of The National Academy Of Sciences Of The United States Of America* **109,** 20820–20825 (2012).

16. Köhler, S., Schmoller, K. M., Crevenna, A. H. & Bausch, A. R. Regulating contractility of the actomyosin cytoskeleton by pH. *Cell Rep.* **2,** 433–439 (2012).

17. Murrell, M., Oakes, P. W., Lenz, M. & Gardel, M. L. Forcing cells into shape: the mechanics of actomyosin contractility. *Nature Reviews Molecular Cell Biology* **16,** 486–498 (2015).

18. Lenz, M. Geometrical Origins of Contractility in Disordered Actomyosin Networks. *Phys. Rev. X* **4,** 041002 (2014).

19. Kruse, K. & Jülicher, F. Actively contracting bundles of polar filaments. *Phys. Rev. Lett.* **85,** 1778–1781 (2000).

20. Foster, P. J., Fürthauer, S., Shelley, M. J. & Needleman, D. J. Active contraction of microtubule networks. *eLife* **4,** e10837 (2015).

21. Torisawa, T., Taniguchi, D., Ishihara, S. & Oiwa, K. Spontaneous Formation of a Globally Connected Contractile Network in a Microtubule-Motor System. *Biophys. J.* **111,** 373–385 (2016).

22. Tan, R., Foster, P. J., Needleman, D. J. & McKenney, R. J. Cooperative Accumulation of Dynein-Dynactin at Microtubule Minus-Ends Drives Microtubule Network Reorganization. *Developmental Cell* **44,** 233–247 (2018).

23. Lenz, M., Thoresen, T., Gardel, M. L. & Dinner, A. R. Contractile units in disordered actomyosin bundles arise from F-actin buckling. *Physical Review Letters* **108,** 238107 (2012).

24. Chen, S., Markovich, T. & MacKintosh, F. C. Motor-Free Contractility in Active Gels. *Phys. Rev. Lett.* **125,** 208101 (2020).

25. Chen, S., Markovich, T. & MacKintosh, F. C. Motor-free contractility of active biopolymer networks. *arXiv preprint arXiv:2204.00222* (2022).

26. Lénárt, P. *et al.* A contractile nuclear actin network drives chromosome congression in oocytes. *Nature* **436,** 812–818 (July 2005).

27. Bun, P., Dmitrieff, S., Belmonte, J. M., Nédélec, F. J. & Lénárt, P. A disassembly-driven mechanism explains F-actin-mediated chromosome transport in starfish oocytes. *eLife* **7,** e31469 (2018).

28. Kučera, O. *et al.* Anillin propels myosin-independent constriction of actin rings. *Nat. Commun.* **12,** 4595 (2021).

29. Fürthauer, S., Needleman, D. J. & Shelley, M. J. A design framework for actively crosslinked filament networks. *New Journal of Physics* **23,** 013012 (2021).

30. Fürthauer, S. *et al.* Self-straining of actively crosslinked microtubule networks. *Nature physics* **15,** 1295–1300 (2019).

31. Bischof, J. *et al.* A cdk1 gradient guides surface contraction waves in oocytes. *Nature Communications* **8,** 1–10 (2017).

32. Klughammer, N. *et al.* Cytoplasmic flows in starfish oocytes are fully determined by cortical contractions. *PLoS Computational Biology* **14,** e1006588 (2018).

33. Wigbers, M. C. *et al.* A hierarchy of protein patterns robustly decodes cell shape information. *Nature Physics* **17,** 578–584 (2021).

34. Hara, K. Cinematographic observation of "surface contraction waves" (SCW) during the early cleavage of axolotl eggs. *Wilhelm Roux' Archiv für Entwicklungsmechanik der Organismen* **167,** 183–186 (1971).

35. Satoh, N. 'Metachronous ' cleavage and initiation of gastrulation in amphibian embryos. *Development, Growth and Differentiation* **19,** 111–117 (1977).

36. Lewis, C. A. Ultrastructure of a fertilized barnacle egg (Pollicipes polymerus) with peristaltic constrictions. *Wilhelm Roux' Archiv für Entwicklungsmechanik der Organismen* **181,** 333–355 (1977).

37. Sardet, C., Speksnijder, J., Inoue, S. & Jaffe, L. Fertilization and ooplasmic movements in the ascidian egg. *Development* **105,** 237–249 (1989).

38. Narumiya, S., Tanji, M. & Ishizaki, T. Rho signaling, ROCK and mDia1, in transformation, metastasis and invasion. *Cancer and Metastasis Reviews* **28,** 65–76 (2009).

39. Bubb, M. R., Senderowicz, A. M., Sausville, E. A., Duncan, K. L. & Korn, E. D. Jasplakinolide, a cytotoxic natural product, induces actin polymerization and competitively inhibits the binding of phalloidin to F-actin. *Journal of Biological Chemistry* **269,** 14869–14871 (1994).

40. Mori, M. *et al.* An Arp2/3 Nucleated F-Actin Shell Fragments Nuclear Membranes at Nuclear Envelope Breakdown in Starfish Oocytes. *Current Biology* **24,** 1421–1428 (2014).

41. Wesolowska, N. *et al.* Actin assembly ruptures the nuclear envelope by prying the lamina away from nuclear pores and nuclear membranes in starfish oocytes. *eLife* **9,** e49774 (2020).

42. Chugh, P. & Paluch, E. K. The actin cortex at a glance. *Journal of Cell Science* **131,** jcs186254 (2018).

43. Tan, T. H. *et al.* Scale-dependent irreversibility in living matter. *arXiv,* arXiv:2107.05701v1 [physics.bio–ph] (2021).

44. Janson, L. W., Kolega, J. & Taylor, D. L. Modulation of contraction by gelation/solation in a reconstituted motile model. *J. Cell Biol.* **114,** 1005–1015 (1991).

45. Murrell, M. & Gardel, M. L. Actomyosin sliding is attenuated in contractile biomimetic cortices. *Mol. Biol. Cell* **25,** 1845–1853 (2014).

46. Belmonte, J. M., Leptin, M. & Nédélec, F. A theory that predicts behaviors of disordered cytoskeletal networks. *Mol. Syst. Biol.* **13,** 941 (2017).

47. Gardel, M. L. *et al.* Elastic behavior of cross-linked and bundled actin networks. *Science* **304,** 1301–1305 (2004).

48. Yang, X. *et al.* Physical bioenergetics: Energy fluxes, budgets, and constraints in cells. *Proc. Natl. Acad. Sci. U. S. A.* **118,** e2026786118 (June 2021).